Available online at www.sciencedirect.com

SCIENCE DIRECT®

Remote Sensing of Environment 93 (2004) 296–310

Remote Sensing of Environment

www.elsevier.com/locate/rse

A simulation analysis of the detectability of understory burns in *miombo* woodlands

José M.C. Pereira[a,b,*], Bernardo Mota[b], Jeff L. Privette[c], Kelly K. Caylor[d], João M.N. Silva[a], Ana C.L. Sá[a], Wenge Ni-Meister[e]

[a] *Department of Forestry, Instituto Superior de Agronomia, Tapada da Ajuda, 1349-017 Lisboa, Portugal*
[b] *Cartography Centre, Tropical Research Institute, Travessa do Conde da Ribeira 9, 1300-142 Lisboa, Portugal*
[c] *NASA Goddard Space Flight Center, Greenbelt, MD 20771, USA*
[d] *Department of Civil and Environmental Engineering, Princeton University, Princeton, NJ 08544, USA*
[e] *Department of Geography, Hunter College of the City University of New York, 695 Park Avenue, New York, NY 10021, USA*

Received 23 May 2003; received in revised form 23 December 2003; accepted 10 January 2004

Abstract

The miombo woodlands of southern Africa are one of the most extensively burned biomes in the tropics. The detectability of understory burns in these woodlands was assessed with a sensitivity analysis approach, based on a hybrid geometrical–optical radiative transfer model. Model input data were obtained from a variety of sources, including field biometry and spectroradiometry, and satellite data. The effects of variable tree percent cover, leaf area index, stand density, burn scar age, illumination and observation geometry, and spectral region, were taken into account. Detectability of understory burns was defined as the spectral separability of burned and unburned understory, measured with the Jeffries–Matusita distance, for all possible combinations of the green, red, and near-infrared channels of the Moderate Resolution Imaging Spectrometer (MODIS) sensor. Single channels, or pairwise combinations of channels perform poorly at detecting understory burns, but a large improvement in detectability is obtained for the combination of the three spectral domains. The detectability of understory burns is largely insensitive to the effects of stand structure and illumination/observation geometry, and depends primarily on burn scar age. Our results agree with those of previous satellite-based studies of burns scar detectability in African savanna woodlands.

Keywords: Simulation analysis; Understory burns; Miombo woodlands

1. Introduction

The incidence of fire in Africa exceeds that of every other continent (Pyne, 1997). In an analysis of global fire activity based on 21 months of daily, daytime satellite data at 1-km resolution, Dwyer et al. (2000) determined that about half of the fires detected were located in Africa. Barbosa et al. (1999) estimated that the mean annual area burned in Africa during the period 1985–1991 was in the interval 3.5×10^6 to 6.3×10^6 km^2, while burnt biomass varied in the range 704–2168 Tg. African fire activity is strongly concentrated in the seasonally wet tropics (van Wilgen & Scholes, 1997), which have a hot, wet season lasting between 4 and 8 months, and a dry season during the rest of the year. The dominant vegetation type in these areas of high fire frequency is woodland, defined as land with an open stand of trees the crowns of which form a canopy from 8 to 20 m or more in height, and that cover at least 40% of the surface. The field layer tends to be sparse, dominated by grasses, and usually with little foliage between the grass stratum and the lower canopy (White, 1983). Tropical savanna woodland fires in Africa, South America, Southeast Asia, and Australia typically burn this understory layer and do not consume the tree crowns. The objective of the present study is to assess the detectability of understory burns in southern Africa savanna woodlands, taking into consideration the spectral and structural properties of the tree stands and of the surface vegetation layer, before and after the fire.

* Corresponding author. Department of Forestry, Instituto Superior de Agronomia, Tapada da Ajuda, 1349-017 Lisboa, Portugal.
E-mail addresses: jmcpereira@isa.utl.pt (J.M.C. Pereira), bmota@isa.utl.pt (B. Mota), jeff.privette@gsfc.nasa.gov (J.L. Privette), kcaylor@princeton.edu (K.K. Caylor), joaosilva@isa.utl.pt (J.M.N. Silva), anasa@isa.utl.pt (A.C.L. Sá), wenge@geo.hunter.cuny.edu (W. Ni-Meister).

0034-4257/$ - see front matter © 2004 Elsevier Inc. All rights reserved.
doi:10.1016/j.rse.2004.01.009

The research reported was developed under the auspices of the SAFARI 2000 international research initiative, and its field activities took place during the Third Intensive Field Campaign, in the dry season of 2000 (Swap et al., 2002, 2003).

1.1. Canopy reflectance modelling

The detectability of understory burns is analyzed with a canopy reflectance modeling approach (Goel, 1988; Asner et al., 2003). Canopy reflectance models (CRM) are mathematical representations of the physics of the interaction between solar radiation, vegetation elements, and background surface, and relate plant canopy and background characteristics to their spectral reflectance signature. Goel (1988, 1989) considers four categories of CRM, namely geometrical models, turbid-medium models, hybrid models, and computer simulation models. Turbid-medium models are particularly appropriate to model the reflectance of dense, horizontally uniform plant canopies, such as agricultural crops, and thus were not considered suitable for our purposes. Computer simulation models track the interaction between radiation and the vegetation canopy almost on a photon-by-photon basis, making this kind of CRM very realistic. However, we lacked the data to parameterize these complex models, which are too computationally intensive for the simulation analysis approach followed in this study.

Geometrical models describe the canopy as set of geometrical objects with given shapes, dimensions, and optical properties, laid out in a specified pattern, and overlying a ground surface of known reflective characteristics. Canopy reflectance is determined by the interception of light and shadowing by the geometrical objects, and reflectance from the sunlit and shadowed fractions of the background surface. Hybrid models combine the geometric optics (GO) of large-scale canopy structure with principles of radiative transfer (RT) for volume scattering within individual crowns. Hybrid GORT models are appropriate to model discontinuous natural vegetation canopies, which exhibit gaps and openings (Li & Strahler, 1992), and are relatively simple to parameterize and validate (Ni et al., 1999).

1.2. Remote sensing of the understory layer

Caetano et al. (1998b) assessed the importance of nonlinear spectral mixing between a pine forest overstory and a shrub understory layer using a hybrid GORT model. They unmixed overall canopy reflectance into three components: a forest canopy component, a shrub background component, and a background-canopy mixed component. Caetano et al. (1998a) developed an approach for characterizing the forest understory, based on the shrub background component and on standard forest inventory data.

Boschetti et al. (2003) used a radiative transfer model to simulate and analyze canopy spectral signature changes for varying overstory leaf area index (LAI) and diverse understory conditions, in a sparse canopy poplar plantation. Based on this analysis, the ability of a spectral index using short wave infrared data to minimize understory influence on overall scene reflectance was assessed.

Other studies relied on satellite imagery to analyze forest understory. Hall et al. (2000) produced maps of conifer understory within deciduous-dominated mixed stands. They used Landsat Thematic Mapper imagery, combined with stand inventory data, and achieved an accuracy of 71% in understory type mapping. Wilson and Ference (2001) analyzed the spectral separability of various understory components, including four ecological indicator plant species. Spectral mixture analysis of Compact Airborne Spectrographic Imager (CASI) imagery successfully separated understory and overstory spectral components, and showed that canopy closure plays a major role in the detectability of understory characteristics.

In spite of the prevalence of understory fires in tropical savannas, disturbed tropical evergreen forests (Cochrane et al., 1999; Nepstad et al., 1999) and their common occurrence in temperate and boreal forests (Brown & Davis, 1973), there appears to be a complete lack of research on the detectability of burnt surfaces as a function of overstory characteristics, illumination and observation geometry, and fire scar age.

1.3. Study area

In southern Africa, fire incidence is particularly high in the wetter Zambezian miombo woodlands of eastern Angola, northern Zambia, southwestern Tanzania and central Malawi (Frost, 1996). Wetter miombo is characteristic of areas with mean annual precipitation higher than 1000 mm, but less when occurring on Kalahari sand (White, 1983). Canopy height of these woodlands often exceeds 15 m in height. Floristically, the arboreal layer of miombo woodlands is dominated by *Brachystegia* sp., either alone or in conjunction with *Julbernardia* sp. or *Isoberlinia* sp. The miombo is distinctive because of the shape of its dominant trees, which have mostly short and slender boles. Branches start as sharply ascending, then spread out to support light, shallow, flat-topped crown, with pinnate leaves (White, 1983). One of the characteristic features of miombo woodland is its uniformity over wide areas, which is due to physiognomic similarities of the dominant canopy trees, and to similarity of environmental conditions across the region (Desanker et al., 1997).

Our study area is the wetter Zambezian miombo woodland, corresponding to mapping unit 25 of White (1983), located in southern hemisphere Africa approximately between 4°S and 16°S, and between 14°E and 40°E. The types of miombo woodland stand structure simulated in this study are meant to be representative of the vegetation in that area. Haanpää (1998) combined data from various authors, and compiled a calendar of miombo phenological seasons. The aspects most relevant for modelling the detectability of

Table 1
Fire season in miombo woodlands

<table>
<tr><th>May</th><th>Jun</th><th>Jul</th><th>Aug</th><th>Sep</th><th>Oct</th><th>Nov</th></tr>
<tr><td colspan="7">Fires occur</td></tr>
<tr><td></td><td></td><td></td><td colspan="3">Peak fire season</td><td></td></tr>
<tr><td></td><td></td><td></td><td></td><td colspan="2">Hot late dry season</td><td></td></tr>
<tr><td colspan="4">Cool early dry season</td><td></td><td></td><td></td></tr>
<tr><td></td><td></td><td colspan="3">Peak leaf fall</td><td></td><td></td></tr>
</table>

Modified from Haanpää (1998).

understory fires are summarized in Table 1. Most miombo trees are deciduous, shedding leaves during the dry season. Leaf fall peaks in August–September in the wetter miombo. Dry season understory fires are a regular, frequent occurrence, especially during the months of August to October (Frost, 1996).

2. Data and methods

2.1. Geometric optical and radiative transfer (GORT) modelling

The issue of detectability of burns in the understory of miombo woodlands was analyzed in a forward simulation approach, using an analytical hybrid geometric optical (GO) and radiative transfer (RT) model (Ni et al., 1999). In forward modeling, scene reflectance is simulated using hypothetical and/or measured leaf, canopy and stand characteristics, to analyze the effects of forest structure on spectral reflectance signatures (Asner et al., 2003). We did not to attempt to model actual miombo woodland, but compiled the required data from a variety of sources, and simulated a range of plausible stand structures. The analytical hybrid GORT model of Ni et al. (1999) combines the geometric optics of large-scale canopy structure with principles of radiative transfer for volume scattering within individual crowns. Pure GO models capture the essential structure of discontinuous plant canopies, namely the clumping of leaves into crowns, which cast shadows. The area in the field of view of a sensor is modeled as a mix of sunlit and shaded crowns and background (Ni et al., 1999). The analytical approximation of radiative transfer was used to model multiple scattering between leaves, within individual crowns. The RT component accounts for the influence of the optical properties of the foliage on multiple scattering (Ni et al., 1999). Model input parameters are:

– Illumination, θ_I, and viewing, θ_V, zenith angles.
– Tree and stand geometry parameters:
– vertical crown radius, r_v (m)
– horizontal crown radius, r_h (m)
– stand density, n (m^{-2})
– height of averaged crown center, h (m)
– difference of upper bound and lower bound of crown centers, Δh (m).
– foliage area volume density, F_a ($m^2\ m^{-3}$)
– Spectral signature data:
– leaf single scattering albedo, ω (dimensionless)
– background reflectance, ρ_s (dimensionless)

The analytical hybrid GORT treats a scene as the combination of four components: sunlit crowns, shaded crowns, sunlit background, and shaded background. The bi-directional reflectance of the whole scene is modeled as the sum of the reflectance of the individual components, weighted by their respective areal proportions (Ni et al., 1999):

$$R(\theta_I, \theta_V, \phi_R) = K_c C + K_g G + K_t T + K_z Z \quad (1)$$

where: ϕ_R = relative azimuth angle; K_c = areal proportion of sunlit and viewed crown; C = spectral signature of sunlit and viewed crown; K_g = areal proportion of sunlit and viewed background; G = spectral signature of sunlit and viewed background; K_t = areal proportion of shaded and viewed crown; T = spectral signature of shaded and viewed crown;

Table 2
Angular values for the early dry season, high stand density, and old fire scar scenario

Case	Solar zenith (θ_I)	View zenith (θ_V)	Solar azimuth[a] (ϕ_I)	View azimuth[a] (ϕ_V)	Relative azimuth (ϕ_R)
□	42.69°	40°	57.11°	270°	147.11°
△	42.69°	25°	57.11°	270°	147.11°
○	42.69°	0°	57.11°	Undefined[b]	Undefined[b]
▲	42.69°	25°	57.11°	90°	32.89°
■	42.69°	40°	57.11°	90°	32.89°

Case symbols correspond to those in Fig. 8.
[a] North corresponds to an azimuth of 0° and South to 180°. The view azimuths of 90° and 270° correspond to off-nadir satellite positions over the 13°S parallel, looking due East and due West, respectively.
[b] The azimuth of a nadir view (view zenith of 0°) is undefined.

Table 3
Angular values for the late dry season, low stand density, and recent fire scar scenario

Case	Solar zenith (θ_I)	View zenith (θ_V)	Solar azimuth[a] (ϕ_I)	View azimuth[a] (ϕ_V)	Relative azimuth (ϕ_R)
□	29.48°	40°	40.45°	270°	130.45°
△	29.48°	25°	40.45°	270°	130.45°
○	29.48°	0°	40.45°	Undefined[b]	Undefined[b]
▲	29.48°	25°	40.45°	90°	49.55°
■	29.48°	40°	40.45°	90°	49.55°

Case symbols correspond to those in Fig. 8.
[a] North corresponds to an azimuth of 0° and South to 180°. The view azimuths of 90° and 270° correspond to off-nadir satellite positions over the 13°S parallel, looking due East and due West, respectively.
[b] The azimuth of a nadir view (view zenith of 0°) is undefined.

K_z = areal proportion of shaded and viewed background; Z = spectral signature of shaded and viewed background.

Ni et al. (1999) and Ni and Li (2000) provide further details about the analytical HGORT model. The overall scene spectral signatures produced as the main model output were used to analyse the separability between burned and unburned understory scenarios and, therefore, to determine the detectability of understory burns.

Ni et al. (1999) and Ni and Li (2000) assessed the accuracy of the analytical HGORT model to simulate the reflectance of a dense black spruce (*Picea mariana*) forest in central Canada, and of an open mesquite (*Prosopis glandulosa*) shrubland in New Mexico, respectively. Model results from the black spruce site were compared with field measurements from the Portable Apparatus for Rapid Acquisition of Bidirectional Observations of Land and Atmosphere (PARABOLA), Advanced Solid-state Array Spectroradiometer (ASAS), and POLarization and Directionality of Earth's Reflectance (POLDER) instruments. Model predictions fit the POLDER and PARABOLA measurements well in the principal plane and across the principal plane, in both the visible and near infrared spectral domains, at a solar zenith angle of 36°. Field measurements were slightly overestimated in the backward scattering direction. At a solar zenith angle of 47.7°, the model fits well the ASAS and PARABOLA measurements along the principal plane, in the visible and near infrared. The analytical HGORT model captured well the bowl shape with a strong hotspot in the backward scattering direction, typical of the bi-directional reflectance of conifer forests in the principal plane (Ni et al., 1999). Ni and Li (2000) compared model results with Advanced Very High-Resolution Radiometer (AVHRR) red and near infrared reflectance measurements in the quasi-principal plane. Model predictions slightly underestimate AVHRR measurements in the backward scattering direction, and slightly overestimate them in the forward scattering direction. The root mean square error (RMSE) is 0.0037 in the red (AVHRR channel 1) and 0.046 in the near infrared (AVHRR channel 2). Model predictions also agreed well with POLDER measurements, with slight overestimation close to the hotspot angle, and slight underestimation at smaller reflectance values in the forward scattering direction.

2.2. Model input data

2.2.1. Illumination and observation geometry

The scene illumination angle for the HGORT simulations depends on latitude of the study area and time of the year. Two dates were considered, corresponding to the early dry season and the late dry season. The dates selected correspond to the first and third quartile of the cumulative distributions of nighttime active fire counts

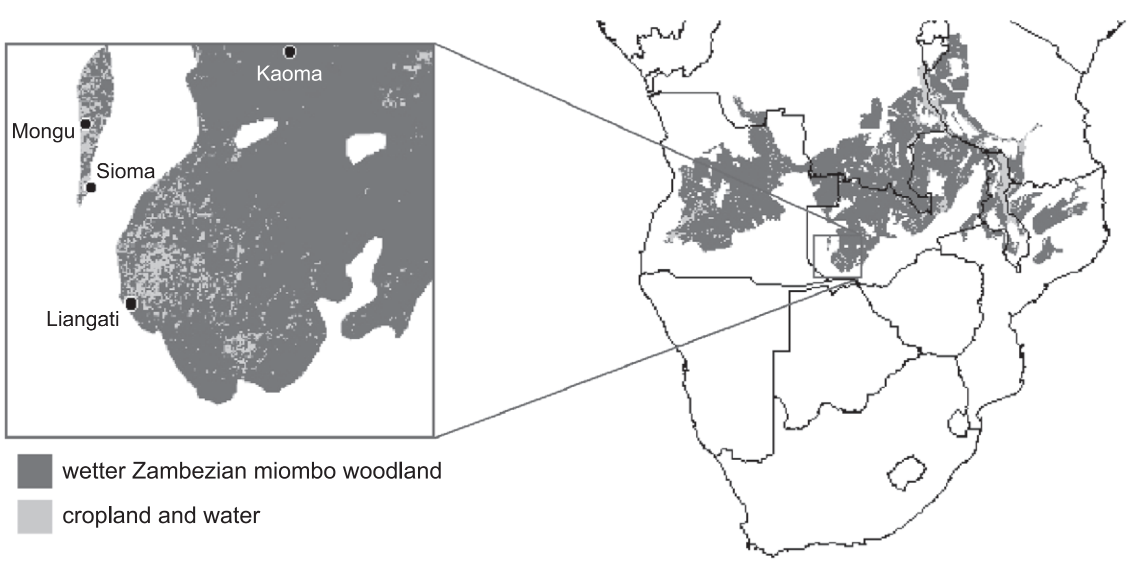

Fig. 1. Miombo woodlands of southern Africa, and study area.

(Arino & Plummer, 2001) from the Along Track Scanning Radiometer (ATSR-2) for the 2000 dry season of southern Africa, and are, respectively, July 3 and September 5. Latitude of 13°S was selected, corresponding to the area where most of the field data used in this study were gathered. The illumination geometry on July 3 and September 5, at 13°S and at 10:30 AM local time (the nominal time of overpass of various Earth observation satellites) and the observation geometry postulated for the simulations are given in Tables 2 and 3.

2.2.2. Tree and stand biometry

Some of the tree geometry parameters were obtained from the field measurements of Scholes et al. (2002), carried out in Zambia at Kataba Forest Reserve, near Mongu, at Liangati Forest Reserve, and at Maziba Bay Forest, near Sioma (Fig. 1). At each of the three sites, the woodland basal area is dominated by *Brachystegia* species. To calculate mean tree and stand structural inputs required by the HGORT model, only live trees with diameter at breast height larger than 5 cm were considered, for a total of 618 trees at the three sites (Scholes et al., 2002). The following tree geometry parameters were obtained from the data:

$r_v = 2$ m
$r_h = 2.3$ m
$h = 5.9$ m
$\Delta h = 4$ m

Stand density and tree foliage area volume density were not measured in the field. Both parameters were estimated through relationships with variables measured in the field,

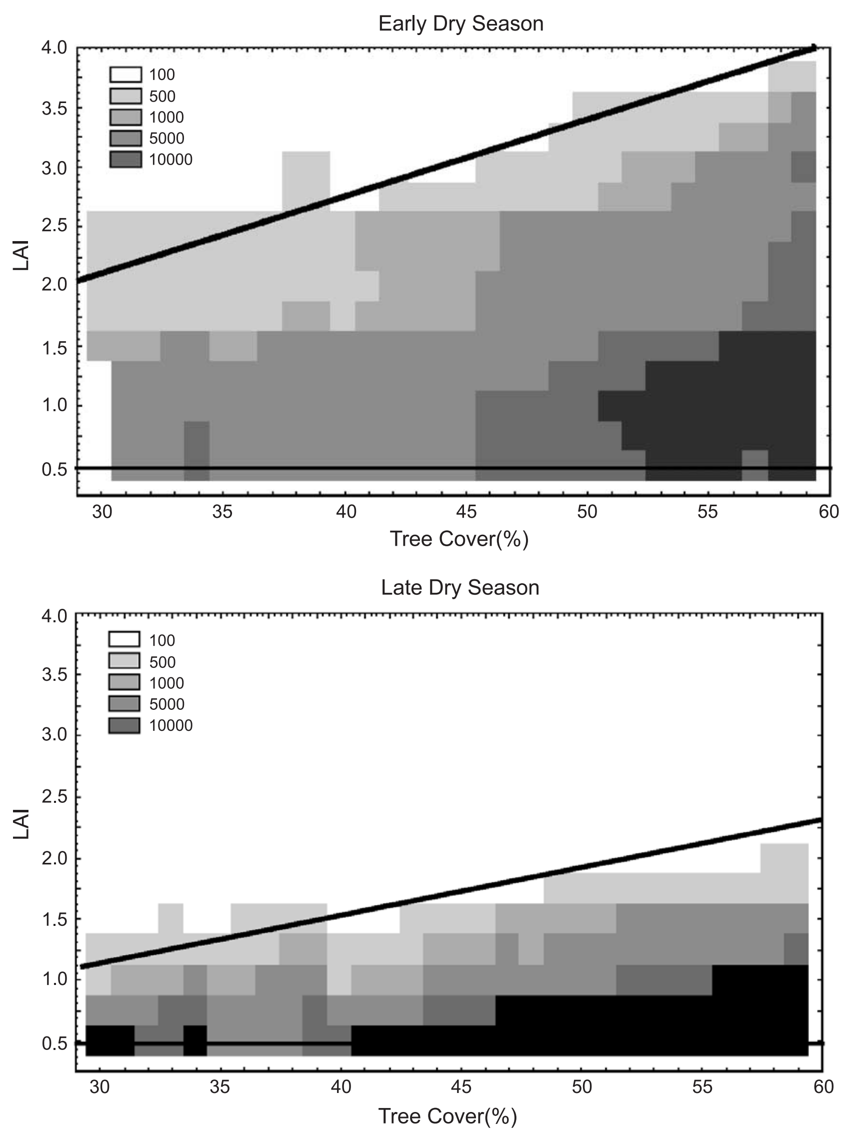

Fig. 2. Scatterplots of tree % cover ($TC_{\%}$) vs. leaf area index (LAI). The solid black lines bound the range of values used in the simulation analysis. The upper bound is the 99th percentile regression line. The gray shade quantifies the number of 1-km Continuous Fields Tree Cover Project and MODIS LAI pixels.

and variables obtained from satellite data. Stand density, n, was calculated from tree percent cover ($TC_{\%}$) data using the following relationship (Woodcock et al., 1997):

$$n = \frac{\ln(1 - TC_{\%})}{\pi r_h^2} \tag{2}$$

where $TC_{\%}$ is tree percent cover, n is stand density (m^{-2}), and r_h is as defined above.

Two values were used for horizontal crown radius. The value of 2.3 m obtained from the data of Scholes et al. (2002) corresponds to a structure with smaller trees and higher stand density, for any given value of tree percent cover. A horizontal crown radius of 3.5 m was taken from the plateau miombo data of Fuller et al. (1997), representing woodland made up of larger trees, forming a less dense stand. These two stand structures are designated as high density, and low density in the simulation analysis. Tree percent cover data were obtained from the University of Maryland Continuous Fields Tree Cover Project (DeFries et al., 2000). Tree foliage area volume density, F_a, was calculated from its relationship with leaf area index (LAI) and $TC_{\%}$. The relationship between LAI and F_a is (Gao et al., 2000):

$$\mathrm{LAI} = F_a \pi r_v n \frac{4}{3} r_h^2 \tag{3}$$

Eqs. (2) and (3) can be combined to yield:

$$F_a = \frac{3\mathrm{LAI}}{4 r_v (\ln(1 - TC_{\%})^{-1})} \tag{4}$$

2.2.3. Tree percent cover and leaf area index data

Tree percent cover data were obtained from the University of Maryland Continuous Fields Tree Cover Project (DeFries et al., 2000), and LAI data were taken from the MOD15A2 MODerate resolution Imaging Spectrometer (MODIS)/Terra LAI Product (Myneni et al., 2001). The $TC_{\%}$ legend ranges from 10% to 80%, in 1% increments. A legend value of 80% actually represents cover equal or greater than 80% and a value of 10% is equal or less than 10% cover. The tree cover map was generated with a linear mixture model approach applied to 1-km Advanced Very High-Resolution Radiometer (AVHRR) data acquired during 1992–1993. The MODIS LAI product is defined as the one-sided green leaf area per unit ground area. The 1-km product used is produced from 8-day composite data, with the selected value in the compositing period corresponding to that with the highest fraction of absorbed photosynthetically active radiation (FPAR). LAI is calculated from atmospherically corrected bi-directional reflectance factors in the 648- and 858-nm MODIS channels (Privette et al., 2002).

White's (1983) vegetation map has a scale of 1:5,000,000 and resulted from the simplification of various larger-scale national or regional vegetation maps published prior to the early 1970s. Given the coarse scale of White's map and the fact that some 30 years have elapsed since the original information was compiled, we updated the limits of mapping unit 25 with data from the University of Maryland 1-km global land cover map (Hansen et al., 2000). The purpose of this operation was to exclude areas of cropland from analysis. The resulting region (dark gray, in Fig. 1) was used as a template to extract the $TC_{\%}$ and LAI data for the study area.

2.2.4. $TC_{\%}$/LAI relationship

Simulation of plausible miombo stand structures requires an analysis of the quantitative relationship between $TC_{\%}$ and LAI, the variables used to calculate the n

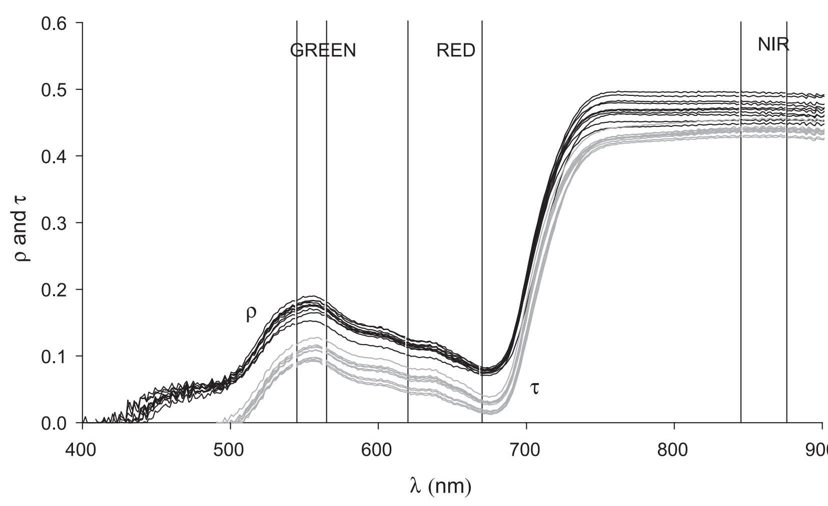

Fig. 3. Spectral reflectance (ρ) and transmittance (τ) signatures of *Brachystegia spiciformis* leaves. The spectral regions used in the simulation analysis are shown.

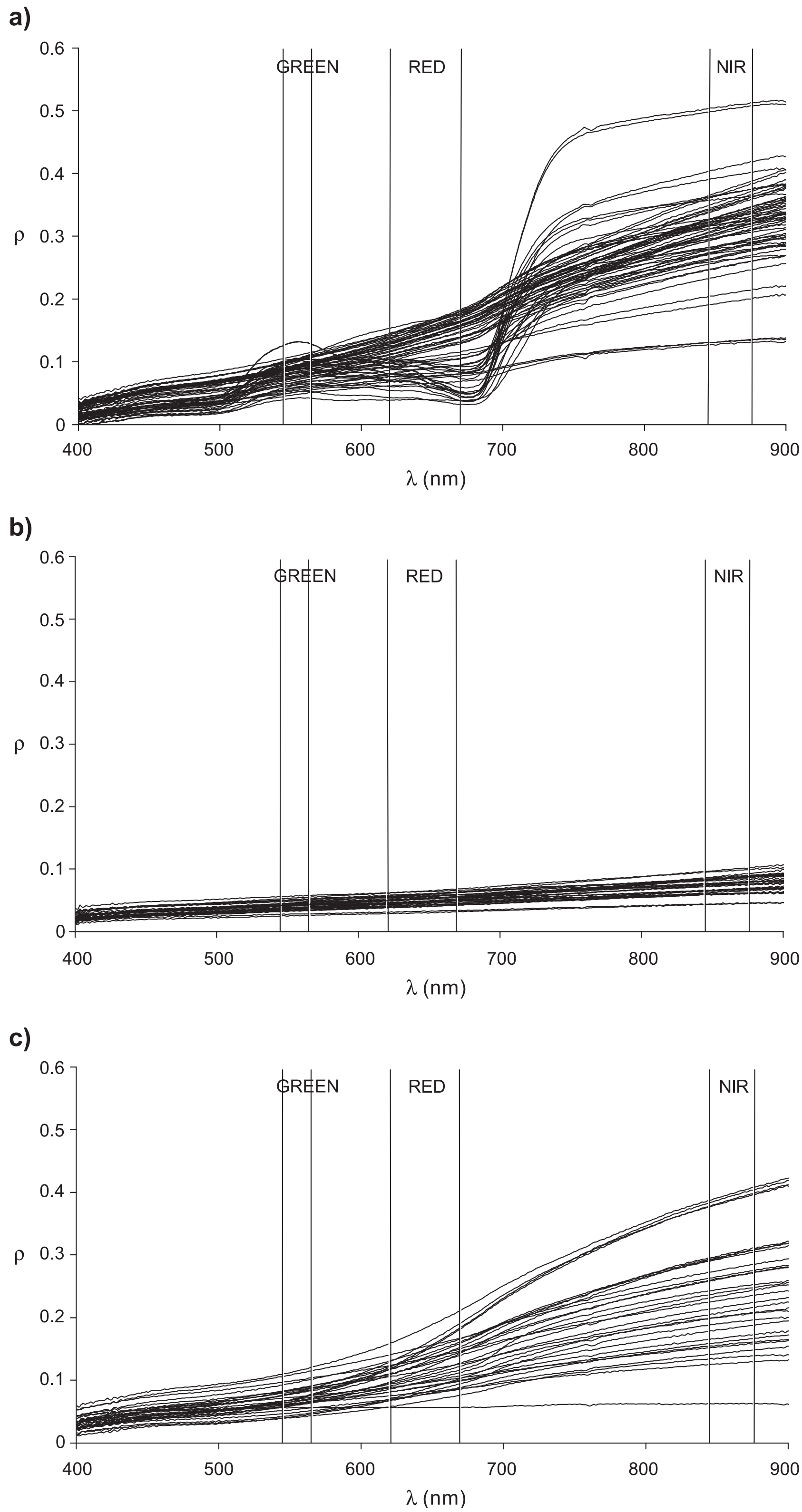

Fig. 4. Spectral reflectance (ρ) signatures of (a) unburned background; (b) recent burn background; (c) old burn background. The spectral regions used in the simulation analysis are shown.

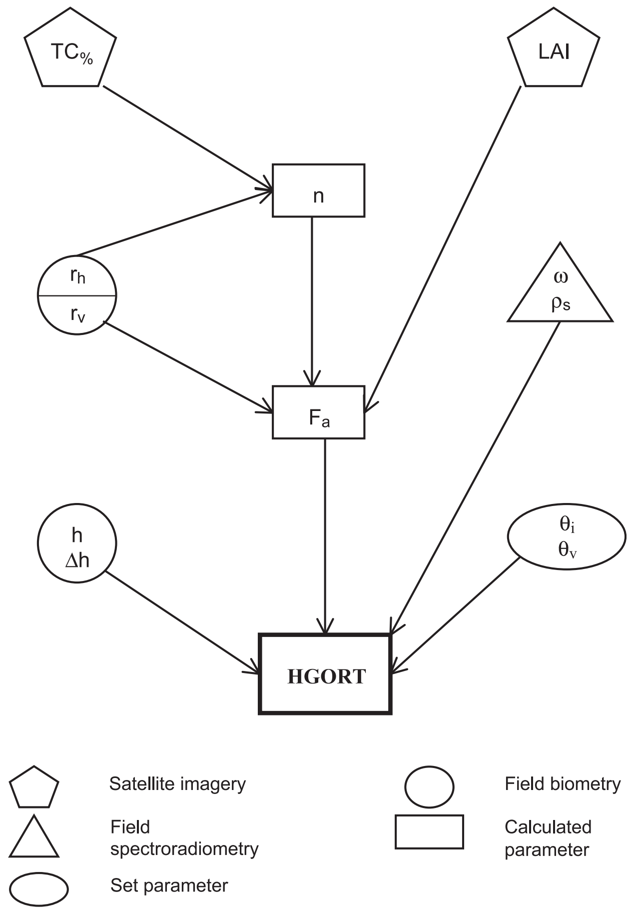

Fig. 5. Relationship between variables and parameters used in the simulation analysis, and respective data sources.

and F_a HGORT inputs. The relationship between $TC_{\%}$ and LAI was analysed with scatterplots where $TC_{\%}$ is plotted as the independent variable, and LAI as the dependent variable (Fig. 2). The scatterplots contain a random sample of 1% of the satellite data, corresponding to 15,286 pixels. Values of $TC_{\%}$ below 30% were excluded from the analysis, because it seemed reasonable to expect that such a low level of tree cover would not affect detectability of understory burns. Values of LAI lower than 0.5 were left out for the same reason (Fig. 2). The upper bound of $TC_{\%}$ is 60%, corresponding to the upper limit of tree cover for the woodland class as defined by DeFries et al. (2000). The triangular nature of the relationship between $TC_{\%}$ and LAI is expected if $TC_{\%}$ is interpreted as a limiting factor constraining LAI. Quantile regression techniques have recently been proposed as a statistically sound technique for determining quantitatively the magnitude of the boundaries of polygonal relationships between two variables, where one variable can be considered the dependent variable (LAI), and the other the independent variable ($TC_{\%}$) (Cade et al., 1999; Scharf et al., 1998). The upper boundary of the relationship was defined at the 99th regression quantile, for both the early and late dry season scatterplots. Thus, the simulation domain in $TC_{\%}$/LAI space is bound by the $TC_{\%}$ values of 30% and 60%, and by the 99th quantile regression line of the relationship between the two variables. Simulated miombo stands were defined at a grid of points with increments of 10% tree cover and of 0.5 LAI, plus the corresponding points falling on the regression line (Fig. 2).

2.2.5. Tree leaf and background spectral data

Spectral measurements were performed near Kaoma, in the Western Province, Zambia. Spectral reflectance (ρ) and transmittance (τ) of tree leaves were measured with a FieldSpec VNIR spectroradiometer (Analytical Spectral Devices, Boulder, CO), coupled to a LI-COR LI1800-12 External Integrating Sphere. Measurements were made over the range 0.4–0.9 μm, with a 1.4-nm sampling interval. Reflectance and transmittance of 10 randomly selected *Brachystegia spiciformis* leaves were measured both on the adaxial and abaxial leaf surfaces. Five measurements were made on each side of each leaf, with 10 replicates for each measurement. Thus, each spectral signature shown in Fig. 3 is the mean of 100 spectral signatures. Single-scattering albedo, ω, is the sum of ρ and τ values. The spectral data used in the simulation analysis correspond to the green, red and near-infrared (NIR) regions shown in Fig. 3, and were obtained via convolution of the spectral signatures shown, with the respective MODIS filter response functions.

Background reflectance, ρ_s was measured with the FieldSpec VNIR spectroradiometer at four separate woodland sites near Kaoma. At the beginning of each set of measurements, the reflectance of a white Spectralon reference plate was measured, to estimate solar irradiance at the surface and allow for the calculation of reflectance factors. Two of the sites had not been burned during the 2000 dry season. At the first of these sites, dry grass and leaf litter dominated the understory. Scattered shrubs with senescing leaves were also present. The second unburned site was relatively open woodland, with a predominantly shrubby understory. Dry grass and leaf litter were also present, but covered a smaller area than at the first site. Shrub foliage was green, and new foliage was beginning to emerge. The other two sites where background reflectance was measured had been burned during the 2000 dry season. The first site had burned 2 days earlier, and large fallen logs were still smoldering. The understory vegetation was thoroughly burned and significant quantities of ash were deposited on the ground. Tree crown scorching displayed very variable height, but had not affected a significant volume of the canopy. There was little leaf litter, scorched or otherwise, at the surface. The second site had been burned 3 to 4 weeks earlier. Leaf litter was abundant, made up mostly of scorched leaves. Exposed soil surface was clearly visible, but some areas were still blackened by a charcoal deposit. At all sites, care was taken to make surface reflectance measurements under canopy clearings, to avoid the interference of tree shading, and of radiance transmitted through the tree crowns. Reference plate measurements were taken at nearby large clearings. Fig. 4 shows the spectral signatures of background reflectance. The spectral data used in the simulation analysis correspond to the green, red and near-infrared (NIR) regions shown in Fig. 4, and were obtained by convolving the spectral signatures shown, with the corresponding MODIS filter response functions.

2.2.6. Simulation design and detectability of understory burns

The relationship between the various types of input data and parameters is shown in Fig. 5. Different values of input parameters were combined, resulting in a large number of model runs. Each run was parameterized by a pair of $TC_{\%}$ and LAI values, date (early vs. late dry season), stand density (low vs. high), type of understory (unburned, recent burn, old burn), and spectral region (green, red, NIR). Spectral variability of the understory was addressed by performing 60 simulation runs for each understory type, using a different spectral signature measured in the field, for each run. The total number of simulation runs performed for each pair of $TC_{\%}$/LAI values was 1080. The number of $TC_{\%}$/LAI pairs is 24 for the early dry season, and 15 for the late dry season, yielding a total of 42,120 simulation runs. In order to contain a combinatorial explosion of cases, angular effects were analyzed only for two extreme cases. The first corresponds to the late dry season, under low tree density and with a recently burned surface, a combination of factors that is expected to result in a relatively high detectability of the understory burn. The second case simulates an early dry season scenario, with high tree density and an older burn, and is expected to correspond to lower detectability of the understory burning. The total

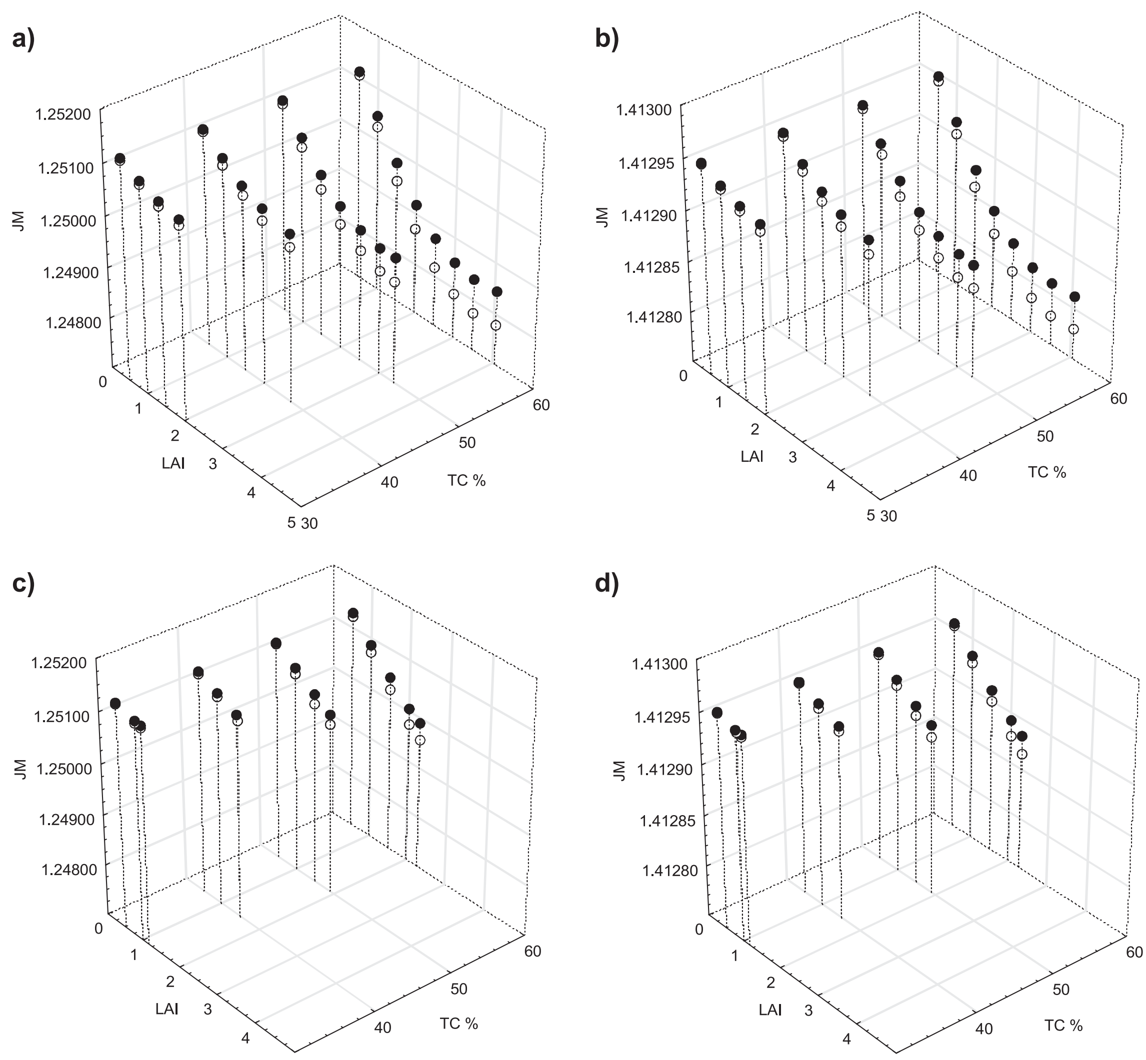

Fig. 6. Jeffries–Matusita distance as a function of $TC_{\%}$ and LAI, for the following simulation cases: (a) early dry season, old burn; (b) early dry season, recent; (c) late dry season, old burn; (d) late dry season, recent burn. Black circle: low-density stand. White circle: high-density stand.

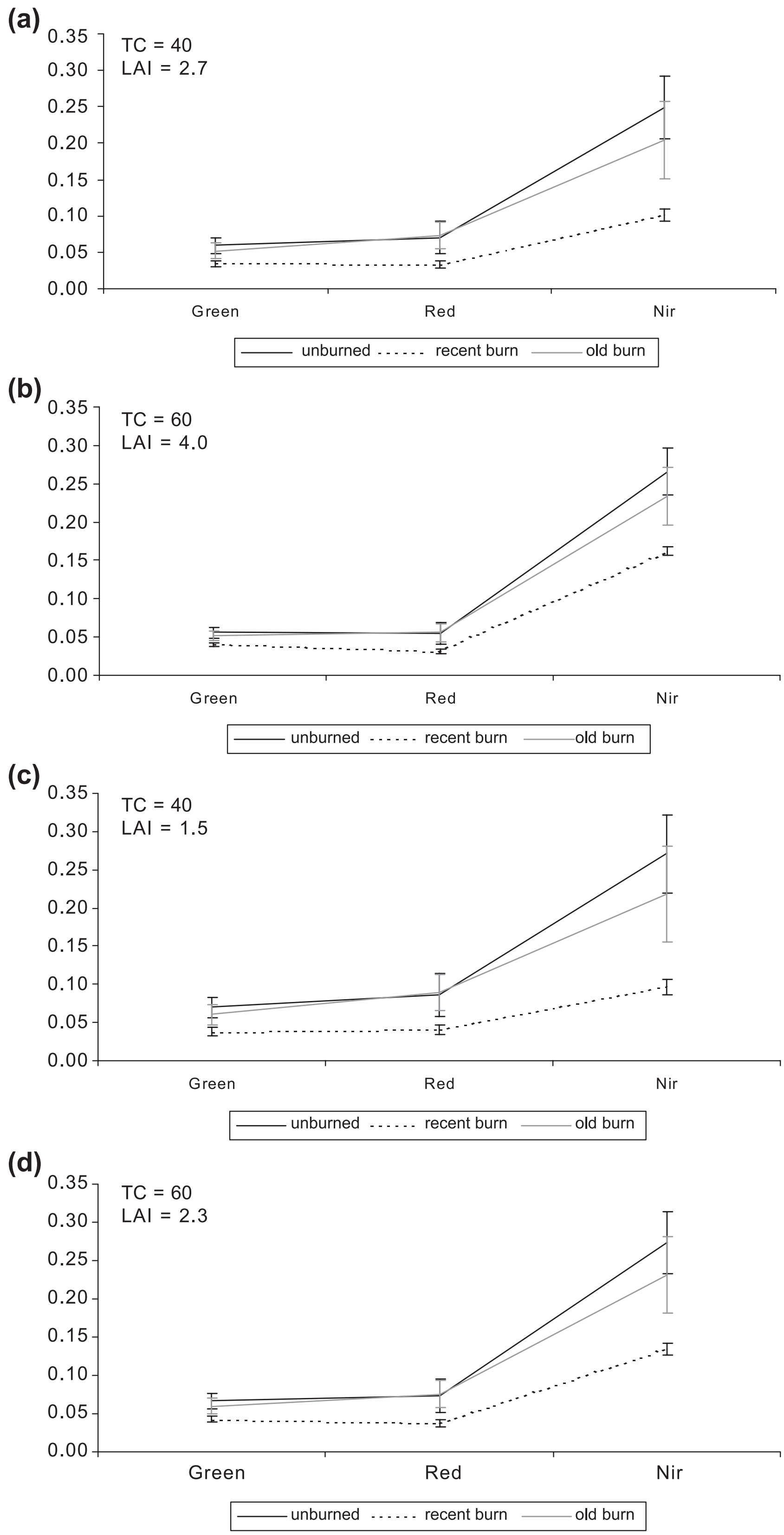

Fig. 7. Model output spectral signatures, R (θ_I, θ_V, ϕ_R), for various points along the 99th percentile regression line of Fig. 2. (a and b) early dry season; (c and d) late dry season. The JM distances between unburned and old burn for the green–red–NIR signatures are: (a) 1.250; (b) 1.248; (c) 1.251; (d) 1.250. The JM distances between unburned and recent burn for the green–red–NIR signatures are at the maximum of 1.414 in all cases.

number of simulation runs for the analysis of angular effects was 70,200. Tables 2 and 3 show values for θ_I, θ_V, ϕ_I, ϕ_V, and ϕ_R for the 10 illumination/observation geometry scenarios simulated.

The detectability of burns in the understory of the simulated miombo woodland stands was assessed by comparing the HGORT-generated scene spectral signatures for the unburned understory with those of the recent burn and old burn cases, keeping all other parameters constant. The comparison of signatures was performed using the Jeffries–Matusita (JM) distance, calculated with the green, red, and NIR spectral channels. The JM distance is a saturating transform of the Bhattacharya distance (Jensen, 1996):

$$\mathrm{JM}_{cd} = \sqrt{2(1 - e^{-\mathrm{Bhat}_{cd}})} \tag{5}$$

where c and d are two spectral classes with Gaussian distribution, e is the base of natural logarithms, and Bhat is the Bhattacharya distance:

$$\mathrm{BHAT}_{cd} = \frac{1}{8}(\mathbf{M}_c - \mathbf{M}_d)^T \frac{(\mathbf{V}_c + \mathbf{V}_d)}{2}(\mathbf{M}_c - \mathbf{M}_d) + \frac{1}{2}\ln \frac{\det \frac{\mathbf{V}_c + \mathbf{V}_d}{2}}{\sqrt{\det(\mathbf{V}_c)}\sqrt{\det(\mathbf{V})_d}} \tag{6}$$

where, $\mathbf{M}_c$ and $\mathbf{M}_d$ = mean matrices of spectral classes c and d; $\mathbf{V}_c$ and $\mathbf{V}_d$ = variance–covariance matrices of spectral classes c and d; det = determinant.

There is a strong relationship between the Bhattacharya distance, or the JM distance, and the classification error of two normally distributed classes. Lee and Choi (2000) developed an approach to estimate the error for the Gaussian maximum likelihood classifier from the Bhattacharya distance. We used that approach combined with Eq. (5) to define JM distance spectral signature separability thresholds that correspond to specified levels of classification error probability. A JM distance of 1.09 corresponds to a classification error probability of 10%, while a 5% classification error probability between two spectral signatures requires a JM distance value of 1.24. We designate pairs of spectral signatures that exceed the 1.09 JM distance threshold as separable, or detectable, and those that exceed the 1.24 threshold as highly separable, or highly detectable.

3. Results

Fig. 6a–d shows JM distance between the spectral signature of unburned understory, and the spectral signature of recent and old burns, as a function of LAI and $TC_{\%}$, for the early and late dry season, for the low and high tree density stands, and for recent and old burns. The variation of JM distance as a function of $TC_{\%}$ and LAI follows the expected pattern, decreasing as LAI and $TC_{\%}$ increase. The difference between high density and low density stand structures is insignificant at low levels of LAI, and increases slightly with LAI and $TC_{\%}$. The values of JM distance obtained in the case of recently burned understory (Fig. 6b and d) indicate high separability from the corresponding case with an unburned understory, regardless of woodland stand structure, and over the range of values analyzed. This observation is valid both for the early dry season and late dry season conditions. A significant decrease in JM distance, to values just above the 5% classification error threshold, is observed when comparing the unburned understory with the older burn scenario (Fig. 6a and c). The relationships between variables are identical to those observed for the recent burns, but they reveal somewhat lower detectability of older burns. Both recent burns and old burns

Table 4
Jeffries–Matusita distances between unburned background, and old burns and recent burns

Early Dry Season

Old Burn									Recent Burn						
$TC_{\%}$	**LAI**	**G**	**R**	**N**	**GR**	**GN**	**RN**	**GRN**	**G**	**R**	**N**	**GR**	**GN**	**RN**	**GRN**
30	2.0	0.333	0.142	0.472	0.410	0.373	0.642	**1.251**	**1.221**	**1.153**	**1.389**	**1.359**	**1.320**	**1.414**	**1.414**
40	2.7	0.333	0.142	0.472	0.441	0.394	0.644	**1.250**	**1.221**	**1.153**	**1.388**	**1.361**	**1.331**	**1.414**	**1.414**
50	3.4	0.333	0.142	0.470	0.438	0.381	0.647	**1.249**	**1.221**	**1.153**	**1.388**	**1.371**	**1.337**	**1.414**	**1.414**
60	4.0	0.333	0.142	0.469	0.414	0.386	0.649	**1.248**	**1.221**	**1.153**	**1.387**	**1.370**	**1.343**	**1.414**	**1.414**

Late Dry Season

Old Burn									Recent Burn						
$TC_{\%}$	**LAI**	**G**	**R**	**N**	**GR**	**GN**	**RN**	**GRN**	**G**	**R**	**N**	**GR**	**GN**	**RN**	**GRN**
30	1.1	0.333	0.142	0.473	0.441	0.367	0.640	**1.251**	**1.221**	**1.153**	**1.389**	**1.368**	**1.336**	**1.414**	**1.414**
40	1.5	0.333	0.142	0.473	0.429	0.377	0.642	**1.251**	**1.221**	**1.153**	**1.389**	**1.369**	**1.339**	**1.414**	**1.414**
50	1.9	0.333	0.142	0.472	0.428	0.385	0.644	**1.250**	**1.221**	**1.153**	**1.389**	**1.369**	**1.345**	**1.414**	**1.414**
60	2.3	0.333	0.142	0.471	0.426	0.397	0.645	**1.250**	**1.221**	**1.153**	**1.388**	**1.373**	**1.349**	**1.414**	**1.414**

The tree cover ($TC_{\%}$) and leaf area index (LAI) pairs correspond to the sample points on the 99th percentile regression lines of Fig. 2. Values in bold represent spectral signatures separable with a classification error lower or equal to 10%. Values in bold and underlined represent spectral signatures separable with a classification error lower or equal to 5%. The other values represent cases considered spectrally inseparable. The cases shown in Fig. 7 are shaded.

are slightly more detectable during the late dry season because of the semi-deciduous nature of the wetter Zambezian miombo woodlands, which have lower levels of LAI for any given level of $TC_{\%}$ during that time of the year.

Fig. 7 shows the overall scene spectral signatures produced with HGORT, for four cases along the 99th percentile regression line that defines the boundary of the limiting relationship between the two variables, i.e. at almost the highest LAI level observed for a given $TC_{\%}$ value. Considering the three-dimensional green–red–NIR spectral signatures, the JM distance between recent burns and the unburned scenario is maximal (JM = 1.414) for all $TC_{\%}$ vs. LAI pairs at all wavelengths. The spectral separability between older burns and the unburned scenario is near the 5% classification error threshold. Table 4 displays JM distances between the unburned background, and the old burn and recent burn backgrounds for the sample points shown in Fig. 7, and for four additional points also located along the 99th percentile regression lines in Fig. 2. The table displays JM distances based on all possible combinations of the spectral domains analyzed. No single-channel or two-channel combination provides an acceptable level of detectability in the case of old burns. The better pairwise combination of channels is the red–NIR, but the corresponding JM distance ranges between 0.640 and 0.649, far below the 1.09 threshold required for acceptable separability. Recent burns are more easily discriminated form unburned cases. The 1.09 JM distance threshold is always exceeded, and the 1.24 JM threshold is also exceeded by the NIR channel, as well as by all pairwise combinations of channels. The red–NIR pair, and the green–red–NIR combinations exhibit the maximum JM value of 1.414.

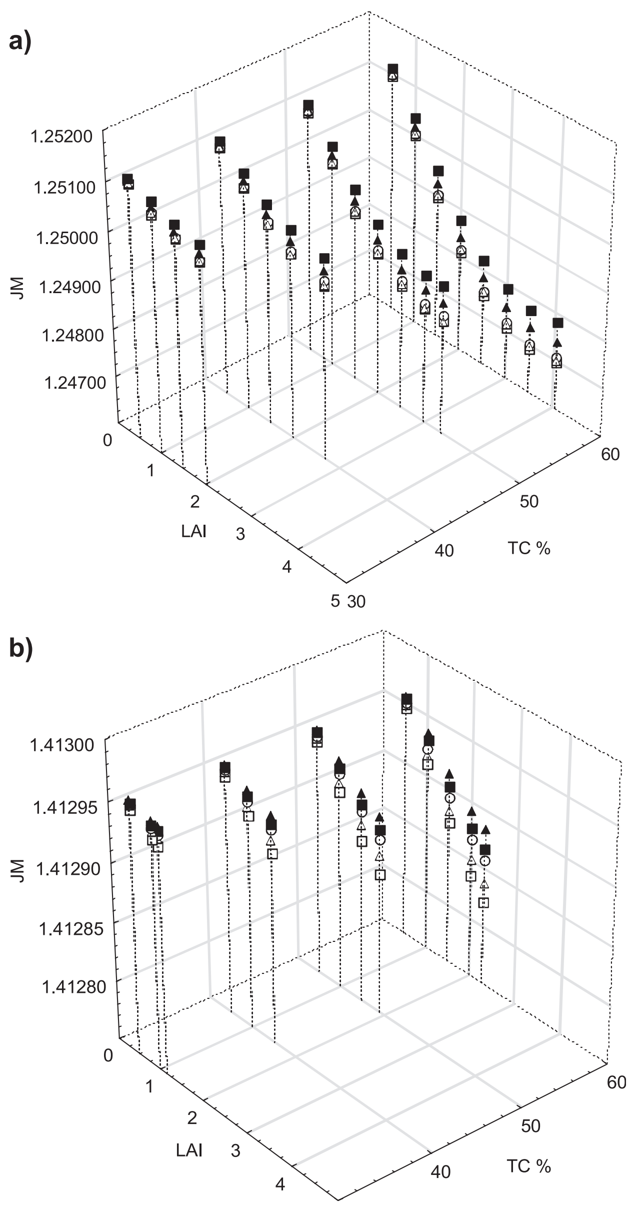

Fig. 8. J–M distance for illumination/observation scenarios: (a) early dry season, high stand density, and old burn; (b) late dry season, low stand density, and recent burn. The symbols correspond to the cases described in Tables 2 and 3.

Fig. 8a shows the detectability of understory burns in the early dry season, high stand density, and old fire scar scenario, as a function of illumination and viewing geometry. At very low LAI values, there is little sensitivity to angular variations. Angular effects increase with LAI and $TC_{\%}$, and JM distance is more sensitive to LAI than to $TC_{\%}$ variation. Spectral separability of understory burns is higher when the satellite is located in the backscatter direction (ϕ_V of 270°, in Tables 2 and 3 than in the forward scatter direction (ϕ_V of 270°, in Tables 2 and 3). Under a ϕ_V of 90°, K_t and K_z are lower than under the other scenarios, thus reducing the confusion between charcoal and shadow, which have similar spectral signatures. Of the two backscatter views, highest separability is attained for the ϕ_V of 40°, which is closest to the θ_I of 42.69° and yields the lower K_t and K_z. Fig. 8b (late dry season, low stand density, and recent burn) displays similar results but with higher separability, due to the presence of a stronger charcoal signature and reduced canopy interception of radiation. In this case maximum separability is obtained for the backscatter view position at a 25° ϕ_V, which is closest to the 29.48° ϕ_I.

4. Discussion and conclusions

Analysis of the spectral detectability of understory burns in a range of miombo woodland stand structures revealed that recently burned sites are clearly separable from unburned sites, using spectral data in the green, red, and NIR domains. Discrimination of older burns is also feasible, although with slightly lower accuracy. Simulation results are highly insensitive to variation in stand structure parameters, and respond almost exclusively to differences in the spectral characteristics of the simulated scene background. Analysis of two illumination/observation geometry cases revealed that spectral separability of understory burns increases as the geometric conditions approach the hotspot situation.

Our results agree with the findings of Fuller et al. (1997), who analyzed the influence of canopy strata on the remotely sensed signal of savanna woodlands from eastern Zambia. They found that the understory layer dominated the remotely sensed signal throughout most of the seasonal cycle, due to the high tree canopy transmittance, inhomogeneous tree cover, and lower reflectance of the tree layer relative to the grassy understory. Their simulations, performed with the SAIL model (Verhoef, 1984) suggest that the tree canopy layer makes a relatively small contribution to landscape-scale normalized difference vegetation index (NDVI), for tree cover values of up to 60%. The tree layer tends to be relatively more important during the dry season, when at least part of the understory vegetation is senescent. Franklin et al. (1991) also reported high canopy transmittance values, ranging from 54% to 87.5%, in savanna trees from the Sudanian and Sahelian bioclimatic zones in Mali, West Africa.

Eva and Lambin (1998) analyzed the spectral separability between burnt areas and unburnt savanna, fragmented forest, and dense humid forest in the Central African Republic. Their comparison was based on all channels from the Landsat Thematic Mapper (TM), the Système Probatoire d'Observation de la Terre multispectral sensor (SPOT-XS), and the Along Track Scanning Radiometer (ATSR-1), and was quantified with the JM distance. To facilitate comparison, we converted their JM distance values reported on a 0–2 scale, to the 0–1.414 scale used in our study. They found that new burns are always highly separable (JM = 1.411–1.414) from the other land cover types, using all spectral channels. Older burns are slightly less separable from unburnt savanna, especially with SPOT-XS data (JM = 1.36). Analysis of the temporal evolution of the spectral contrast between burned areas and unburned woodland savanna, using all ATSR-1 channels (1.6, 3.7, 11, and 12 μm) revealed that JM distance ranges from 1.414 immediately after the fire to 1.25 17 days after the fire, and about 1.1 five weeks after the fire. These spectral separability results obtained from satellite data agree closely with those we obtained. However, it is important to notice that our analysis relied on spectral data from the green, red, and NIR spectral domains and is, therefore, more comparable with the results based on SPOT-XS data than with those from ATSR-1 data, with which it shares no spectral domain.

When studying large areas over long periods of time, it is often necessary to use multitemporal image compositing techniques (Holben, 1986; Qi and Kerr, 1997). The decrease in detectability of burning with time since the fire emphasizes the need to use compositing procedures designed to maximize the fire signal (Sousa et al., 2003; Stroppiana et al., 2002), rather than the standard maximum NDVI criterion (Holben, 1986), which delays detection of the burned area until the next compositing period.

Our simulations were performed based on data representative of the wetter Zambezian miombo woodlands, and a maximum $TC_{\%}$ of 60%. Since spectral detectability of understory burns remains very high even at the highest levels of $TC_{\%}$ tested, it appears reasonable to expect that understory burns will be detectable under higher $TC_{\%}$, and thus that our conclusions may apply beyond mapping unit 25 of White (1983). However, we lack the field spectroradiometry and stand biometry data to rigorously test this hypothesis. The roles of atmospheric effects and spatial pattern of burning were not analyzed in this study. These important issues will be addressed in future research.

Acknowledgements

João M.N. Silva and Ana C.L. Sá were funded by the Foundation for Science and Technology, Ministry for Science and Technology, through doctoral grants SFRH/BD/1026/2000 and SFRH/BD/891/2000, respectively. This research was performed under project POCTI/CTA/33582/99, (*Reduction of uncertainties in estimates of atmospheric emissions from fires in southern Africa*), Foundation for Science and Technology, Ministry for Science and Higher Education, Portugal. We thank Dr. Chris Justice, Department of Geography, University of Maryland, for his effort to involve the Portuguese authors in the activities of SAFARI 2000. We are grateful to the Government of Zambia for hosting our activities.

References

Arino, O., & Plummer, S. (2001). *The Along Track Scanning Radiometer World Fire Atlas—Detection of Night–Time Fire Activity: Validation Report*. IGBP-DIS Working Paper #23. Toulouse, France.

Asner, G. P., Hicke, J. A., & Lobell, D. B. (2003). Per-pixel analysis of forest structure: Vegetation indices, spectral mixture analysis and canopy reflectance modeling. In M. A. Wulder, & S. E. Franklin (Eds.), *Remote sensing of forest environments: Concepts and case studies* (pp. 209–254). Boston, USA: Kluwer Academic Publishing.

Barbosa, P. M., Stroppiana, D., Grégoire, J. -M., & Pereira, J. M. C. (1999). An assessment of vegetation fire in Africa (1981–1991): Burned areas, burned biomass, and atmospheric emissions. *Global Biogeochemical Cycles*, *13*(4), 933–950.

Boschetti, M., Colombo, R., Michele, M., Busetto, L., Panigada, C., Brivio, P. A., Marino, C. M., & Miller, J. R. (2003). Use of semi-empirical and radiative transfer models to estimate biophysical parameters in a sparse canopy forest. In M. Owe, G. d'Urso, & L. Toulios (Eds.), *Remote Sensing for Agriculture, Ecosystems, and Hydrology. Proceedings of The Society of Photo-Optical Instrumentation Engineers (SPIE), vol. 4879* (pp. 133–144). Bellingham, UK: SPIE, The International Society for Optical Engineering.

Brown, A. A., & Davis, K. P. (1973). *Forest fire: Control and use* (2nd ed.). New York, USA: McGraw-Hill.

Cade, B. S., Terrel, J. W., & Schroeder, R. L. (1999). Estimating effects of limiting factors with regression quantiles. *Ecology*, *80*(1), 311–323.

Caetano, M., Huete, A. R., Pereira, J. M. C., & Ni, W. (1998a). Forest understory characterization at regional levels with satellite data: A conceptual approach. In E. T. Engman (Ed.), *Remote Sensing for Agriculture, Ecosystems, and Hydrology. Proceedings of The Society of Photo-Optical Instrumentation Engineers (SPIE), vol. 3499* (pp. 245–256). Bellingham, UK: SPIE, The International Society for Optical Engineering.

Caetano, M., Ni, W., Pereira, J. M. C., & Huete, A. (1998b). Evaluation of the importance of non-linear spectral mixing in coniferous forests. In E. T. Engman (Ed.), *Remote Sensing for Agriculture, Ecosystems, and Hydrology. Proceedings of The Society of Photo-Optical Instrumentation Engineers (SPIE), vol. 3499* (pp. 257–269). Bellingham, UK: SPIE, The International Society for Optical Engineering.

Cochrane, M. A., Alencar, A., Schulze, M. D., Souza, C. M., Nepstad, D. C., Lefebvre, P., & Davidson, E. A. (1999). Positive feedbacks in the fire dynamic of closed canopy tropical forests. *Science*, *284*, 1832–1835.

DeFries, R., Hansen, M., Townshend, J. R. G., Janetos, A. C., & Loveland, T. R. (2000). A new global 1 km data set of percent tree cover derived from remote sensing. *Global Change Biology*, *6*, 247–254.

Desanker, P. V., Frost, P. G. H., Justice, C. O., & Scholes, R. J. (Eds.). (1997). *The Miombo network: Framework for a terrestrial transect study of land-use and land-cover change in Miombo ecosystems of Central AfricaIGBP Report, vol. 41*. Stockholm, Sweden: The International Geosphere-Biosphere Programme (IGBP), 109 pp.

Dwyer, E., Pinnock, S., Grégoire, J. -M., & Pereira, J. M. C. (2000). Global spatial and temporal distribution of vegetation fire as determined from satellite observations. *International Journal of Remote Sensing*, *21*(6), 1289–1302.

Eva, H., & Lambin, E. (1998). Remote sensing of biomass burning in tropical regions: Sampling issues and multisensor approach. *Remote Sensing of Environment*, *64*, 292–315.

Franklin, J., Prince, S. D., Strahler, A. H., Hanan, N. P., & Simonett, D. S. (1991). Reflectance and transmittance properties of West African savanna trees from ground radiometer measurements. *International Journal of Remote Sensing*, *12*(6), 1369–1385.

Frost, P. G. H. (1996). The ecology of miombo woodlands. In B. Campbell (Ed.), *The Miombo in transition: Woodlands and welfare in Africa* (pp. 11–57). Bogor, Indonesia: Center for International Forestry Research (CIFOR).

Fuller, D. O., Prince, S. D., & Astle, W. L. (1997). The influence of canopy strata on remotely sensed observations of savanna-woodlands. *International Journal of Remote Sensing*, *18*(14), 2985–3009.

Gao, X., Huete, A. R., Ni, W., & Miura, T. (2000). Optical–biophysical relationships of vegetation spectra without background contamination. *Remote Sensing of Environment*, *74*, 609–620.

Goel, N. S. (1988). Models of vegetation canopy reflectance and their use in the estimation of biophysical parameters from reflectance data. *Remote Sensing Reviews*, *4*, 1–222.

Goel, N. S. (1989). Inversion of canopy reflectance models for estimation of biophysical parameters from reflectance data. In G. Asrar (Ed.), *Theory and applications of optical remote sensing* (pp. 205–251). New York: Wiley.

Haanpää, M. (1998). Miombo forests—An example of tropical fire ecology. Seminars on Agriculture and Forestry in Developing Countries (MH31) 15th April, 1998. Department of Forest Ecology, Unit of Tropical Silviculture. University of Helsinki, Finland (http://www.lodestone.org/users/maria/misc/miombo.html).

Hall, R. J., Peddle, D. R., & Klita, D. L. (2000). Mapping conifer understory within boreal mixedwoods from Landsat TM satellite imagery and forest inventory information. *Forestry Chronicle*, *76*(6), 887–902.

Hansen, M. C., DeFries, R. S., Townshend, J. G. R., & Sohlberg, R. (2000). Global land cover classification at 1 km spatial resolution using a classification tree approach. *International Journal of Remote Sensing*, *21* (6&7), 1365–1373.

Holben, B. N. (1986). Characteristics of maximum-value composite images from temporal AVHRR data. *International Journal of Remote Sensing*, *7*(11), 1417–1434.

Jensen, J. R. (1996). *Introductory digital image processing: A remote sensing perspective* (2nd ed.). New York: Prentice-Hall.

Lee, C., & Choi, E. (2000). Bayes error evaluation of the Gaussian ML classifier. *IEEE Transactions on Geoscience and Remote Sensing*, *38*, 1471–1475.

Li, X., & Strahler, A. H. (1992). Geometric–optical bi-directional reflectance modeling of the discrete crown vegetation canopy: Effect on crown shape and mutual shadowing. *IEEE Transactions on Geoscience and Remote Sensing*, *30*, 276–292.

Myneni, R. B., Hoffman, S., Knyazikhin, Y., Privette, J. L., Glassy, J., Tian, Y., Wang, Y., Song, X., Zhang, Y., Smith, G. R., Lotsch, A., Friedl, M., Morisette, J. T., Votava, P., Nemani, R. R., & Running, S. W. (2001). Global products of vegetation leaf area and fraction absorbed PAR from year one of MODIS data. *Remote Sensing of Environment*, *83*(1–2), 214–231.

Nepstad, D. C., Veríssimo, A., Alencar, A., Nobre, C., Lima, E., Lefebvre, P., Schlesinger, P., Potter, C., Moutinho, P., Mendoza, E., Cochrane, M., & Brooks, V. (1999). Large-scale impoverishment of Amazonian forests by logging and fire. *Nature 398*, 505–508.

Ni, W., & Li, X. (2000). A coupled vegetation–soil bi-directional reflectance model for a semiarid landscape. *Remote Sensing of Environment*, *74*, 113–124.

Ni, W., Li, X., Woodcock, C. E., Caetano, M. R., & Strahler, A. H. (1999). An analytical hybrid GORT model for bidirectional reflectance over discontinuous plant canopies. *IEEE Transactions on Geoscience and Remote Sensing*, *37*(2), 987–999.

Privette, J. L., Myneni, R. B., Knyazikhin, Y., Mukelabai, M., Roberts, G., Tian, Y., Wang, Y., & Leblanc, S. G. (2002). Early spatial and temporal validation of MODIS LAI product in Africa. *Remote Sensing of Environment*, *83*(1–2), 232–243.

Pyne, S. J. (1997). *World fire: The culture of fire on earth*. Seattle, WA: University of Washington Press, 384 pp.

Qi, J., & Kerr, Y. (1997). On current compositing algorithms. *Remote Sensing Reviews*, *15*, 235–256.

Scharf, F. S., Juanes, F., & Sutherland, M. (1998). Inferring ecological relationships from the edges of scatter diagrams: Comparison of regression techniques. *Ecology*, *79*(2), 448–460.

Scholes, R. J., Dowty, P. R., Caylor, K., Parsons, D. A. B., Frost, P. G. H., & Shugart, H. H. (2002). Trends in savanna structure and composition along an aridity gradient in the Kalahari. *Journal of Vegetation Science*, *13*(3), 419–428.

Sousa, A. M. O., Pereira, J. M. C., & Silva, J. M. N. (2003). Evaluating the performance of multitemporal image compositing algorithms for burned area analysis. *International Journal of Remote Sensing*, *24*(6), 1219–1236.

Stroppiana, D., Pereira, J. M. C., & Grégoire, J. -M. (2002). Radiometric analysis of SPOT-VEGETATION images for burnt area detection in Northern Australia. *Remote Sensing of Environment*, *82*(1), 21–37.

Swap, R. J., Annegarn, H. J., Suttles, J. T., Haywood, J., Helmlinger, M. C., Hely, C., Hobbs, P. V., Holben, B. N., Ji, J., King, M. D., Landmann, T., Maenhaut, W., Otter, L., Pak, B., Piketh, S. J., Platnick, S., Privette, J., Roy, D., Thompson, A. M., Ward, D., & Yokelson, R. (2002). The Southern African Regional Science Initiative (SAFARI 2000): Overview of the dry season field campaign. *South African Journal of Science*, *98*(3–4), 125–130.

Swap, R. J., Annegarn, H. J., Suttles, J. T., King, M. D., Platnick, S., Privette, J. L., & Scholes, R. J. (2003). Africa burning: A thematic analysis of the Southern African Regional Science Initiative (SAFARI 2000). *Journal of Geophysical Research*, *108*(D13), 8465 (doi:10.1029/2003JD003747).

van Wilgen, B. W., & Scholes, R. J. (1997). The vegetation and fire regimes of southern-hemisphere Africa. In B. W. van Wilgen, M. O. Goldammer, J. G. Goldammer, & J. A. Lindesay (Eds.), *Fire in Southern African Savannas: Ecological and atmospheric perspectives* (pp. 27–46). Johannesburg, South Africa: Witwatersrand University Press.

Verhoef, W. (1984). Light scattering by leaf layers with application to canopy reflectance modeling: The SAIL model. *Remote Sensing of Environment*, *16*, 125–141.

White, F. (Ed.). (1983). *The Vegetation of Africa. A descriptive memoir to accompany the UNESCO/AETFAT/UNSO vegetation map of Africa*. Paris: UNESCO, 356 pp.

Wilson, B. A., & Ference, C. G. (2001). The influence of canopy closure on the detection of understory indicator plants in Kananaskis Country. *Canadian Journal of Remote Sensing*, *27*(3), 207–215.

Woodcock, C. E., Collins, J. B., Jakabhazy, V. D., Li, X., Macomber, S. A., & Wu, Y. (1997). Inversion of the Li-Strahler canopy reflectance model for mapping forest structure. *IEEE Transactions on Geoscience and Remote Sensing*, *35*(2), 405–414.